ROYAL SOCIETY
OF CHEMISTRY

PAPER

Check for updates

Chain dynamics and quasi-melting transitions in mixed-halide layered perovskites by NMR spectroscopy

Michael A. Hope [ID] *

Dynamics of the organic cations in hybrid materials can modify the structure and optoelectronic properties, determining the performance in, *e.g.*, photovoltaic devices. In pure-halide BA_2PbI_4 and BA_2PbBr_4, the *n*-butylammonium (BA^+) chains undergo quasi-melting phase transitions at *ca.* −10 °C and 115 °C, respectively, but the chain dynamics in mixed-halide compositions were unknown. Here, we measure the amplitude of motion for each BA^+ carbon as a function of temperature for pure and mixed-halide compositions using $^1H \rightarrow {}^{13}C$ cross-polarisation build-up experiments. We find that motional amplitude increases with temperature with clear steps across the phase transitions in the end-members. Mixed-halide samples exhibit intermediate dynamics, with halide mixing partly or fully suppressing the concerted phase transitions due to the substitutional disorder. This disorder is probed by ^{13}C lineshape analysis, becoming dynamically averaged at high temperature. Using the measured amplitude of motion, the correlation times for motion are calculated from ^{13}C T_1 relaxation as a function of temperature and used to derive the activation energy. This detailed picture of the chain dynamics can inform the design of spacer cations for (mixed-halide) 2D perovskite photovoltaics and passivating layers.

Introduction

Hybrid lead-halide perovskite materials are the subject of intense investigation due to their promising optoelectronic properties for applications including solar cells and LEDs.[1–7] Of these, 2D layered perovskites provide greater stability and structural tunability than their 3D counterparts, finding application as passivating layers on 3D perovskite materials, as well as devices in their own right.[8–14] 2D perovskites comprise perovskite layers of corner sharing lead-halide octahedra separated by bulky organic cations such as butylammonium (Fig. 1). The alkyl chains of the spacers can assume a more ordered arrangement (Fig. 1a), but above a certain temperature a quasi-melting phase transition causes the spacer chains to become more disordered and dynamic,[15–24] which is reflected in the atomic displacement parameters measured by single-crystal X-ray diffraction (XRD) (Fig. 1b).[16] The chain dynamics modulate the physical and optoelectronic properties including the dielectric constant, electronic density of states, and carrier lifetimes;[21,23,25,26] as such, it is important to measure and understand the spacer dynamics in order to design layered perovskites for efficient optoelectronic devices.

A commonly used spacer for layered perovskites and passivating coatings is *n*-butylammonium (BA^+). BA_2PbI_4 has a transition temperature of *ca.* −10 °C, so the spacers are in the

Department of Chemistry, University of Warwick, Coventry, CV4 7AL, UK. E-mail: michael.hope.1@warwick.ac.uk
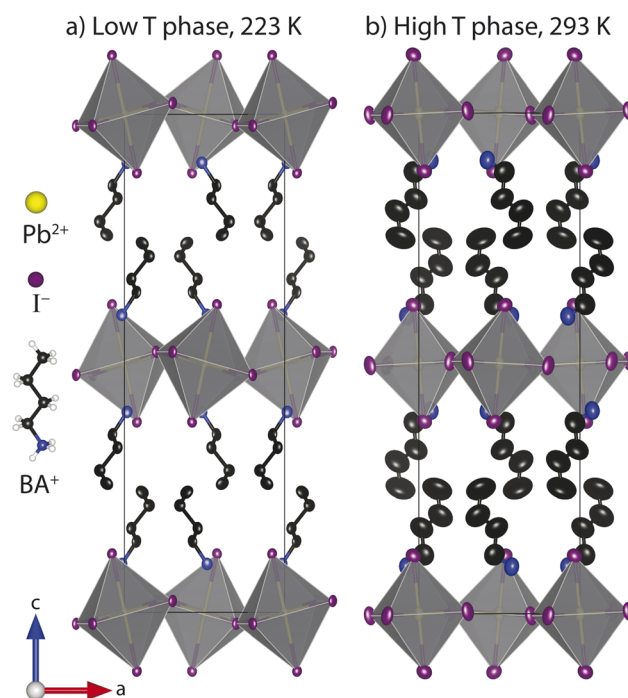
Fig. 1 Crystal structures of BA_2PbI_4 determined by single-crystal XRD below (a) and above (b) the quasi-melting phase transition showing the atomic displacement parameters as ellipsoids. Based on Cambridge Crystallographic Data Centre (CCDC) entries 665689 and 665690.[16]

This journal is © The Royal Society of Chemistry 2025

J. Mater. Chem. A, 2025, **13**, 40153–40165 | **40153**

melted state at room temperature.[16,18,19] In contrast, BA_2PbBr_4 undergoes the melting transition at ~115 °C.[22] For mixed-halide compositions, the spacer dynamics and the presence of any phase transitions is as yet unknown. This is a key factor to consider for the use of mixed-halide layered perovskites, which are of particular interest for their suppressed photoinduced halide segregation.[27–30] However, single-crystal X-ray diffraction experiments are not amenable to mixed-halide samples due to the difficulty in growing large single crystals and the intrinsic local disorder induced by halide mixing.

Solid-state NMR spectroscopy is sensitive to the rate and amplitude of dynamic motion across a broad range of time-scales, without the need for long-range order.[31] Solid-state NMR has been applied to answer a variety of questions for lead-halide perovskites,[32–34] including the fast rotational dynamics of the A-site cation in 3D perovskites,[35–39] dimensionality and methylammonium (MA^+) dynamics in quasi-2D $BA_2MA_{n-1}Pb_nI_{3n+1}$ perovskites,[40–42] phenylethylammonium (PEA^+) ring-flips in $PEA_2MA_{n-1}Pb_nI_{3n+1}$,[43] and halide ordering in mixed-halide 2D perovskites.[44] The dynamics of organic spacer cations can be studied *via* the ^1H–^{13}C dipolar coupling, which depends on the orientation of the C–H bond with respect to the magnetic field: reorientation of the C–H bond vector modulates the ^1H–^{13}C dipolar coupling. Chain dynamics have previously been explored in the room temperature phases of BA_2PbBr_4 and BA_2PbI_4 by measuring ^{13}C T_1 relaxation, which is induced by the ^1H–^{13}C dipolar coupling fluctuations.[25,26] ^1H–^{13}C dipolar coupling can be measured using a variety of experiments;[31] one method is to measure the dipolar oscillations as a function of $^1H \rightarrow ^{13}C$ cross polarisation (CP) contact time.[45–47] The drawback of the CP build-up experiment is that homonuclear ^1H–^1H coupling and spin diffusion suppresses the ^1H–^{13}C dipolar oscillations; homonuclear ^1H coupling can be removed to first order in the Lee–Goldburg CP (LGCP) experiment whereby the ^1H magnetisation is spin-locked along the magic angle during the CP transfer, allowing the ^1H–^{13}C dipolar coupling to be measured with greater precision.[48,49] In this work, $^1H \rightarrow ^{13}C$ CP and LGCP experiments are used to measure the amplitude of BA^+ chain dynamics as a function of temperature in pure and mixed-halide $BA_2Pb(Br_{1-x}I_x)_4$ layered perovskites, including changes in the chain dynamics change across the quasi-melting phase transitions in the end-members and the effect of halide mixing on the phase transitions. Variable temperature ^{13}C spectra reveal halide disorder and its dynamic averaging in the mixed-halide samples. Finally, using the measured amplitude of motion, the correlation times for motion are calculated from ^{13}C T_1 relaxation as a function of temperature and used to derive the activation energy. Together, a detailed picture of the spacer cation chain dynamics in $BA_2Pb(Br_{1-x}I_x)_4$ layered perovskites is established.

Results and discussion

$BA_2Pb(Br_{1-x}I_x)_4$ powder samples were prepared by mechanosynthesis as previously reported[44] and phase purity was confirmed by powder X-ray diffraction (Fig. S1). To identify the quasi-melting transition of the butylammonium chains,

differential scanning calorimetry (DSC) was measured for each sample (Fig. 2). The pure-halide BA_2PbI_4 and BA_2PbBr_4 end members show clear transitions, the temperatures of which are shown in Table 1, consistent with prior literature.[16,19,21,22,41] The transition enthalpies are shown in Table S1. The iodide homologue exhibits a 30 °C hysteresis, while the bromide
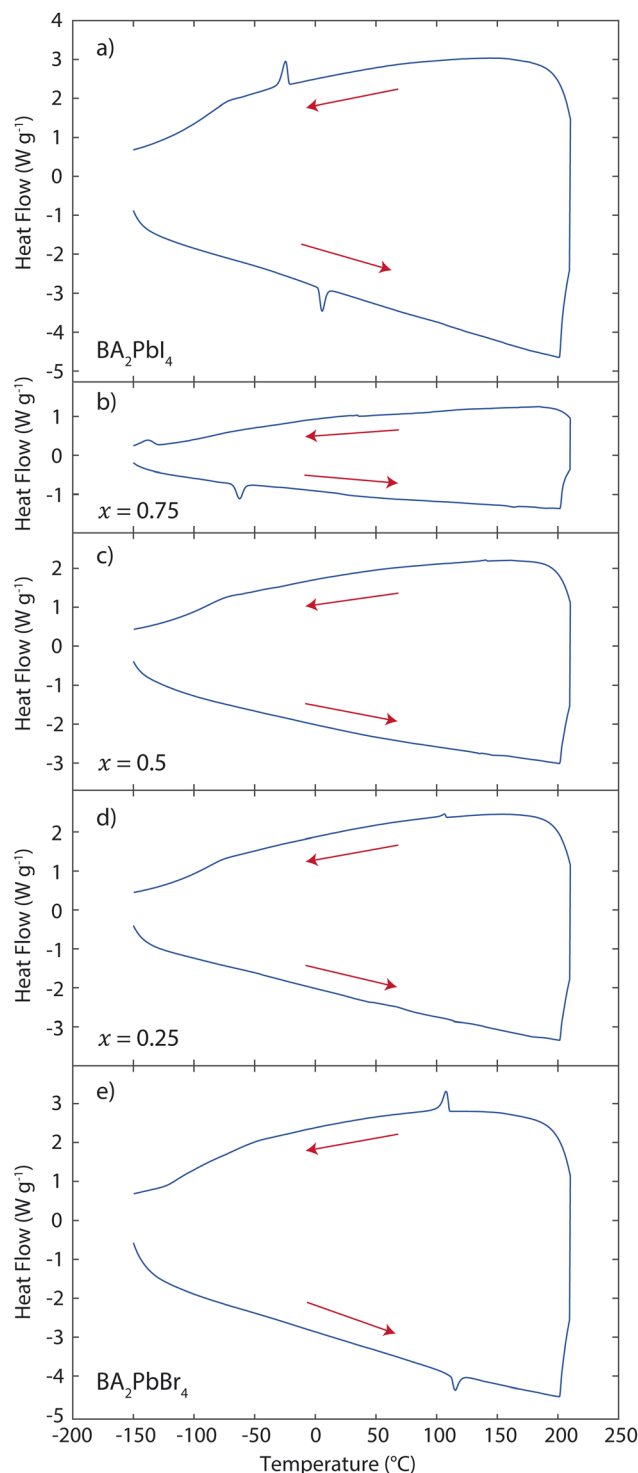

Fig. 2 DSC of $BA_2Pb(Br_{1-x}I_x)_4$ samples for $x = 0$, 0.25, 0.5, 0.75, 1, measured at 20 K min^{-1}.

40154 | *J. Mater. Chem. A*, 2025, **13**, 40153–40165

This journal is © The Royal Society of Chemistry 2025

Table 1 Phase transition temperatures of $BA_2Pb(Br_{1−x}I_x)_4$ samples as determined from DSC (Fig. 2) and jumps in the ^{13}C chemical shift (Fig. 3 and 4). Errors from DSC are estimated from two repetitions of the heating run, those for NMR represent the temperature gradients present within the rotor

$T/°C$	DSC		NMR	
	Cooling	Heating	Cooling	Heating
BA_2PbI_4	$−24 \pm 1$	5 ± 1	$−31 \pm 2$	5 ± 2
BA_2PbBrI_3	$−138 \pm 3$	$−65 \pm 3$	—	—
$BA_2PbBr_2I_2$	—	—	—	—
BA_2PbBr_3I	106 ± 3	113 ± 3	—	—
BA_2PbBr_4	108 ± 1	115 ± 1	106 ± 10	109 ± 10

exhibits a smaller hysteresis of 8 °C. BA_2PbBrI_3 ($x = 0.75$) shows a phase transition at a significantly lower temperature with a large 73 °C hysteresis, BA_2PbBr_3I ($x = 0.25$) shows a very weak transition at the same temperature as pure bromide, and BA_2-$PbBr_2I_2$ ($x = 0.5$) shows no obvious transition in the studied range. This shows that halide mixing disrupts the concerted quasi-melting transition of the BA^+ chains, completely, partly, or by suppressing to far lower temperature. However, questions remain: How dynamic are the BA^+ chains in the mixed-halide samples? Do they more closely resemble the frozen or quasi-melted phases of the end-members? And how do the dynamics depend on temperature in the absence of concerted transitions? Answering these questions requires a local probe of the chain motion.

Fig. 3 shows the $^1H \rightarrow {}^{13}C$ CP NMR spectra of BA_2PbI_4 as a function of temperature. On passing through the quasi-freezing transition, a jump in the ^{13}C shifts is observed, as expected for a first-order transition, with the largest change for the methyl (δ) carbon.[41] Fig. S2 shows the phase fraction determined from the peak integrations as a function of temperature. The transition hysteresis is reproduced, with transition temperatures of $−31$ °C and 5 °C on cooling and heating, respectively (Table 1). The transition temperature on heating is in good agreement with DSC and previous literature. The values on cooling differ between DSC and NMR; however, the degree of hysteresis is known to vary between samples and methods, and both the NMR and DSC values lie within the range of reported literature values ($−33$ to $−17$ °C).[16,18] Fig. 4 shows the variable-temperature $^1H \rightarrow {}^{13}C$ NMR spectra of BA_2PbBr_4. A similar jump in the ^{13}C shifts is observed with transition temperatures of 106 °C and 109 °C on cooling and heating (Table 1 and Fig. S2), in agreement with the DSC data.

To quantify the amplitude of the BA^+ chain dynamics, the ^1H–^{13}C dipolar coupling was measured for each carbon. In the absence of any motion, the dipolar coupling constant can be calculated from the C–H bond length as $D_{rigid} = 23.3$ kHz. Any reorientation of the C–H bond vector on a timescale faster than D_{rigid} reduces the effective ^1H–^{13}C dipolar coupling, D; the greater the range of orientations the C–H vector samples, the smaller the averaged dipolar coupling, reaching zero for uniform wobbling within a hemisphere or sphere (or other specific motions, *e.g.*, rotation about the magic angle). For the
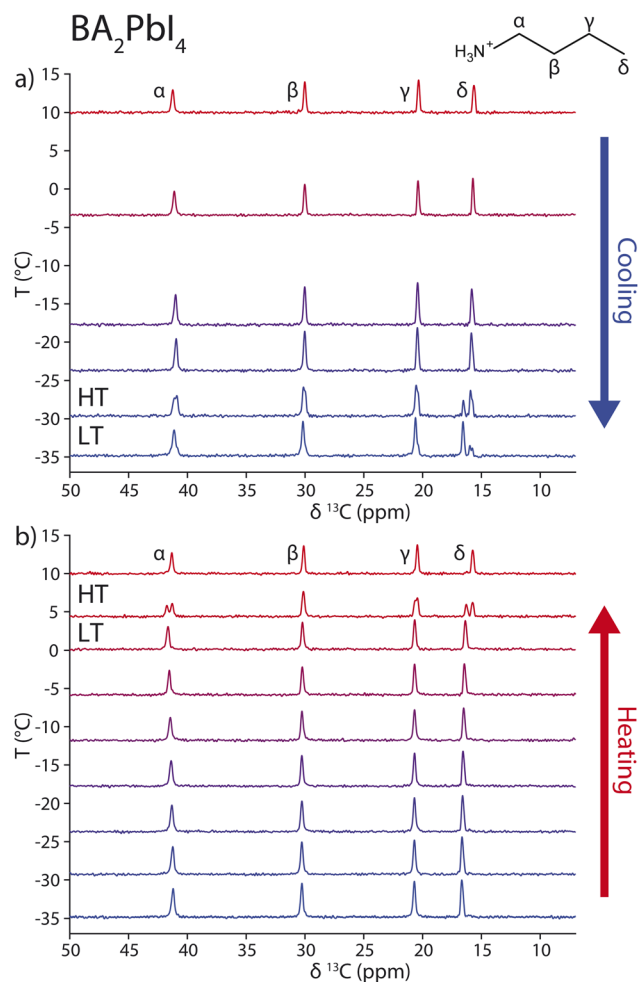

Fig. 3 $^1H \rightarrow {}^{13}C$ CP spectra of BA_2PbI_4 as a function of temperature (a) on cooling and (b) on heating, showing the hysteretic phase transition between the low-temperature (LT) and high-temperature (HT) phases. Spectra were recorded at 11.7 T and 8 kHz magic angle spinning (MAS) rate with a 1 ms contact time.

methyl (δ) carbon, fast C_3 rotation reduces the ^1H–^{13}C dipolar coupling by a factor of three,[50] giving an effective rigid limit of $D_{rigid}^{CH_3} = 7.8$ kHz; any chain reorientation further reduces the dipolar coupling. The magnitude of the chain dynamics can be quantified for each carbon *via* the order parameter, $S = D/D_{rigid}$.

This order parameter quantifies any motion that causes reorientation of the C–H bonds and hence averaging of the ^1H–^{13}C dipolar coupling. For BA^+ within a layered perovskite, this can include rotation about the long axis of BA^+, wobbling of the whole molecule within a cone of a given cone angle (constrained by bonding of the ammonium end to the inorganic layer), rotation about each C–C bond—noting that moving progressively away from the ammonium end, each bond rotation gives a greater degree of freedom—and libration of each bond. These kinds of motions can be seen in molecular dynamics simulations, for instance of the related $BA_2MAPb_2I_7$.[24] However, with a single measurable for each carbon, these motions cannot be distinguished, and therefore the order parameter is considered directly as an unbiased measure of the motional amplitude.
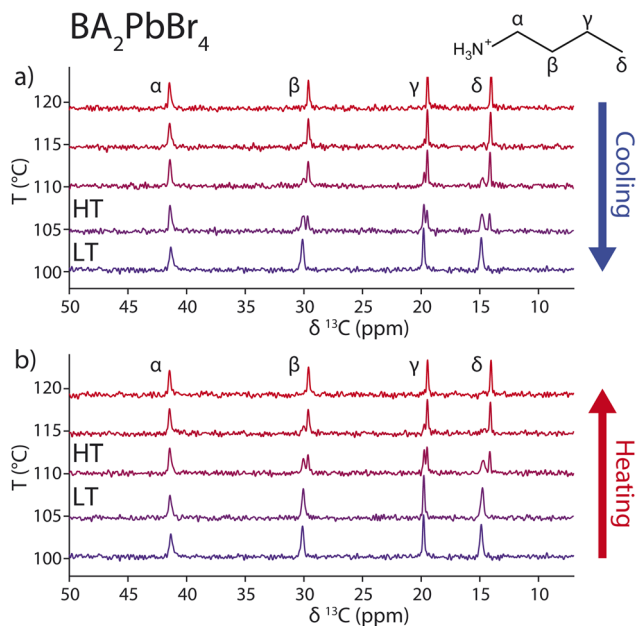
This journal is © The Royal Society of Chemistry 2025

J. Mater. Chem. A, 2025, **13**, 40153–40165 | **40155**

Fig. 4 ^{1}H→^{13}C CP spectra of BA$_2$PbBr$_4$ as a function of temperature (a) on cooling and (b) on heating, showing the phase transition between the low-temperature (LT) and high-temperature (HT) phases. Spectra were recorded at 11.7 T and 8 kHz MAS with a 1 ms contact time.

This is effectively a model-free approach to study the chain dynamics.[51]

Fig. 5a shows the ^{1}H→^{13}C CP build-up curves for BA$_2$PbI$_4$ in the low-temperature phase at −40 °C. Magnetisation transfers quickly for the –CH$_2$– groups (α, β, γ), while build-up is slower for the –CH$_3$ due to the fast C$_3$ rotation. For all carbons, the signal plateaus and dipolar oscillations cannot be readily distinguished, due to equilibration of magnetisation *via* ^{1}H–^{1}H spin diffusion. To reduce ^{1}H–^{1}H spin diffusion during CP, LGCP was used (Fig. 5b), enabling dipolar oscillations to be distinguished for the –CH$_2$– carbons out to 1 ms.

The dipolar coupling was determined by fitting the CP and LGCP build-up curves using SIMPSON.[52] Decay of the dipolar oscillations was accounted for phenomenologically with an exponential damping function for both CP and LGCP (see Experimental); as expected, the decay constants (T_{damp}) are longer for LGCP, due to reduced ^{1}H–^{1}H spin diffusion. The fitted dipolar coupling constants are shown in Fig. 5 and Table S3. There is good agreement between the fitted and experimental data for the –CH$_2$– groups, especially for LGCP; the poorer agreement for the –CH$_3$ carbon could be due to the effect of coupling to the adjacent –CH$_2$– protons, but fitting of the initial build-up is sufficient to determine the dipolar coupling with reasonable accuracy. Where the oscillations decay rapidly (*i.e.*, requiring a short T_{damp}), the CP build-up gives a smaller
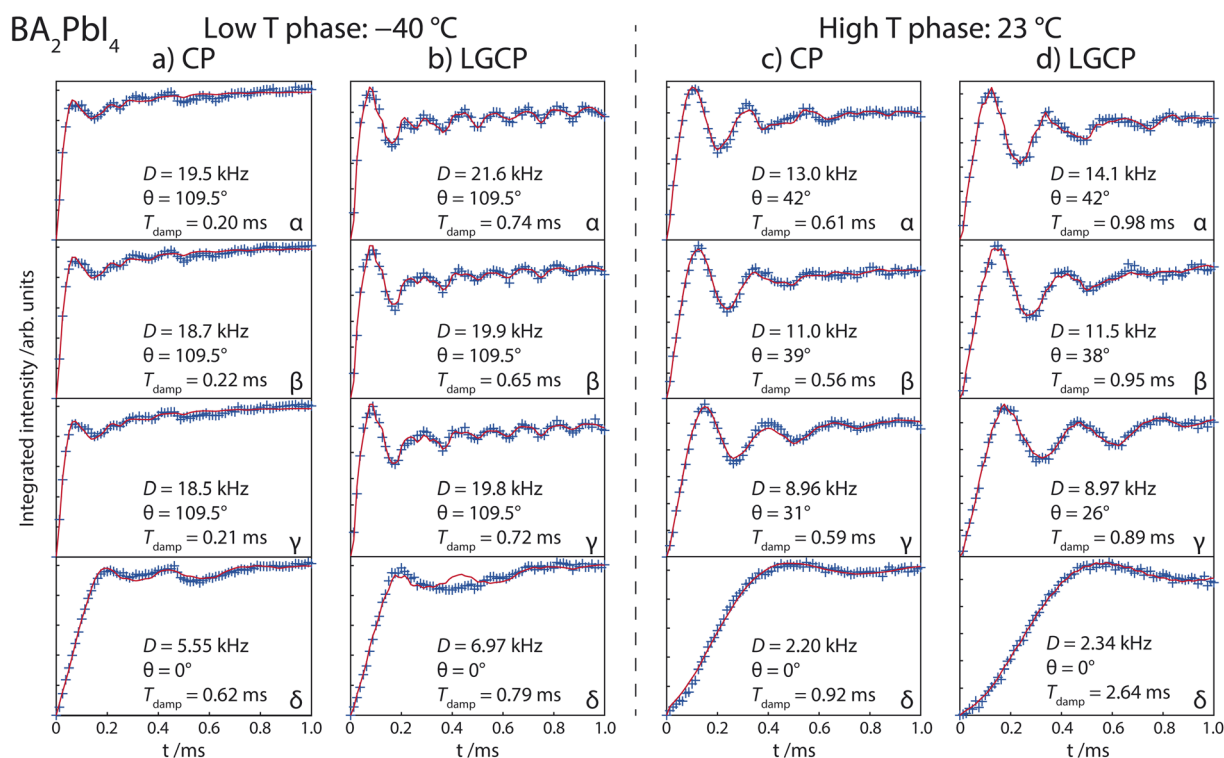

Fig. 5 Integrated intensity as a function of the ^{1}H→^{13}C CP or LGCP contact time for each carbon in BA$_2$PbI$_4$, above and below the quasi-melting phase transition. Experimental data are shown with blue crosses and fitted simulations with red lines. The carbons are labelled α–δ where α is the –CH$_2$– adjacent to the –NH$_3$ and δ is the –CH$_3$ group. Spectra were recorded at 11.7 T and 8 kHz MAS. Simulations were calculated using SIMPSON with the fitted parameters shown: D is the ^{1}H–^{13}C dipolar coupling, θ is the effective angle between the principal axes of the two –CH$_2$–^{1}H–^{13}C dipolar tensors, and T_{damp} is the time constant of the exponential decay applied to the simulated data.

40156 | *J. Mater. Chem. A*, 2025, **13**, 40153–40165

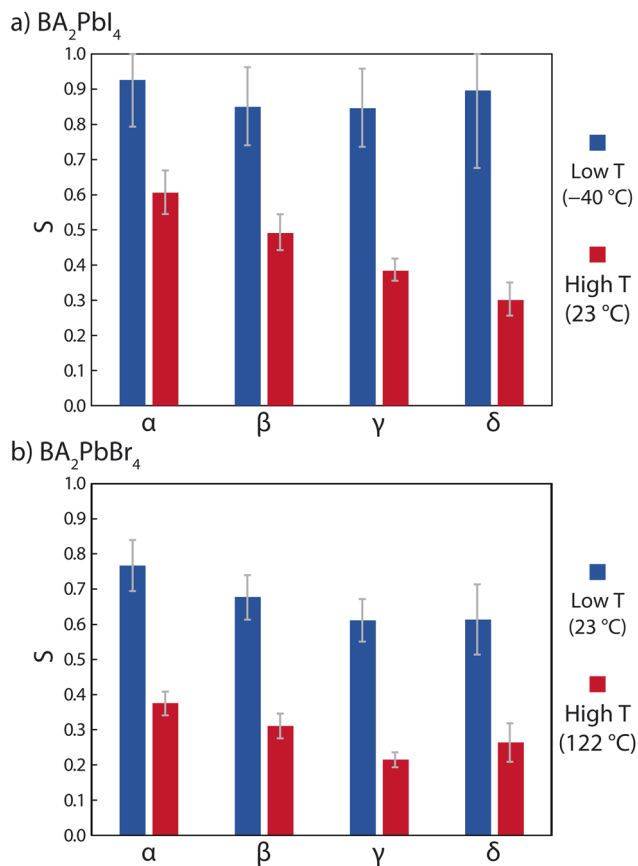This journal is © The Royal Society of Chemistry 2025

Fig. 6 ^{1}H–^{13}C order parameters, S, for (a) BA_2PbI_4 and (b) BA_2PbBr_4 measured by fitting the LGCP build-up, above and below the quasi-melting phase transitions (Fig. 5 and 7). The carbons are labelled α–δ where α is the –CH$_2$– adjacent to the –NH$_3$ and δ is the –CH$_3$ group.

fitted dipolar coupling than the LGCP, whereas LGCP is expected to give a more accurate value. Miscalibration of the LGCP power can lead to scaling errors, however the CP and LGCP values agree within ~10%, ruling out a large LGCP scaling error. The fitted dipolar coupling constants are close to the rigid limit, with order parameters $S \approx 0.9$ (Fig. 6a and Table S3). This indicates that the BA^+ chains are frozen, with only slight librational motion, as expected in the low-temperature phase.

Fig. 5c and d shows the ^{1}H→^{13}C CP and LGCP build-ups for BA_2PbI_4 in the high-temperature phase at 23 °C. The significantly slower build-up and oscillations indicate smaller dipolar coupling constants, providing direct evidence of greater chain dynamics for BA^+ above the quasi-melting transition. Fitting the –CH$_2$– build-up curves with a 109.5° angle between the ^{1}H–^{13}C dipolar tensors, as was the case in the low-temperature data above, gives poor agreement with experiment (Fig. S3). This is because the partial averaging of each dipolar tensor induced by the chain motion changes its effective orientation, and hence the relative orientation between the two tensors. Consequently, the angle between the tensors was allowed to refine during the fitting procedure, yielding good agreement with experiment (Fig. 5, S3 and Table S4). Note that the fast C$_3$ rotation of the methyl group causes all three ^{1}H–^{13}C dipolar tensors to become coaxial (aligned along the C–C bond), so the averaged tensors

remain coaxial regardless of the chain motion. The fitted dipolar coupling constants yield much smaller order parameters for all carbons (Fig. 6a and Table S4), reflecting the greater mobility of the alkyl chains above the melting transition. The order parameter decreases from carbon α–δ moving away from the ammonium group; this is consistent with the ammonium group being bound to the inorganic layer, while rotation about each successive C–C bond increases the flexibility of the moiety.

A similar effect is observed in the ^{1}H→^{13}C (LG)CP build-ups of BA_2PbBr_4, comparing the frozen phase at room temperature and the quasi-melted phase at 122 °C (Fig. 6b and 7, Tables S5 and S6). Some chain motion is already observed at room temperature, with order parameters of $S = 0.6–0.8$ and effective angles between the –CH$_2$– dipolar tensors of $\theta < 109.5°$. Above the quasi-melting transition, the chains become even more dynamic, with a noted reduction in order parameter for all carbons ($S = 0.2–0.4$). Unlike for BA_2PbI_4, the order parameter for carbon δ is greater than that of γ; this could reflect a difference in the chain motion of the two materials, or that the small –CH$_3$ dipolar coupling is being overestimated due to a contribution from the adjacent –CH$_2$– group. Overall, a clear increase in the amplitude of the chain dynamics is observed in the ^{1}H→^{13}C (LG)CP build-ups of BA_2PbI_4 and BA_2PbBr_4 due to their quasi-melting phase transitions.

Having characterised the chain dynamics and quasi-melting transitions in pure BA_2PbI_4 and BA_2PbBr_4, we now turn to mixed $BA_2Pb(Br_{1−x}I_x)_4$ samples. Fig. 8 shows the ^{1}H→^{13}C CP spectra as a function of temperature for $x = 0.25$, 0.5, and 0.75. From these spectra, a number of observations can be made: (1) unlike the end members, there are no 1st order phase transitions that result in a jump in the ^{13}C chemical shift over this temperature range; this is consistent with the absence or significant suppression of transitions in the DSC (see above; note that the low-temperature transition for $x = 0.75$ is outside the accessible temperature range of the present equipment). (2) At room temperature, the ^{13}C resonances are broader than for the end members, reflecting the distribution of local environments introduced by a (partially) disordered arrangement of halide ions in the inorganic layers. This is most significant for the α carbon because it is closest to the inorganic layer. (3) At room temperature, there are two peaks for the δ carbon, separated by ~0.9 ppm. And (4), the peaks become sharper at higher temperature, the broad α resonance collapses, and the split δ peaks coalesce.

The ratio of the split δ carbon signals depends on the halide composition: the higher the bromide content (lower x), the greater the proportion of the environment with the lower shift. The BA^+ δ carbon sits ~4 Å from the axial halide (Fig. S4); therefore, we assign the two peaks to BA^+ cations adjacent to an axial iodide (higher shift) or an axial bromide (lower shift). Since iodide preferentially occupies the axial site,[44,53–55] there is a greater proportion of the iodide-adjacent environment than would be predicted from the composition alone (we note that the relative intensities are approximately consistent with the ordering parameter of *ca.* +0.5 determined in our previous work[44]). The splitting into two distinct sites arises because the δ carbon has only one nearest halide, whereas the α carbon is
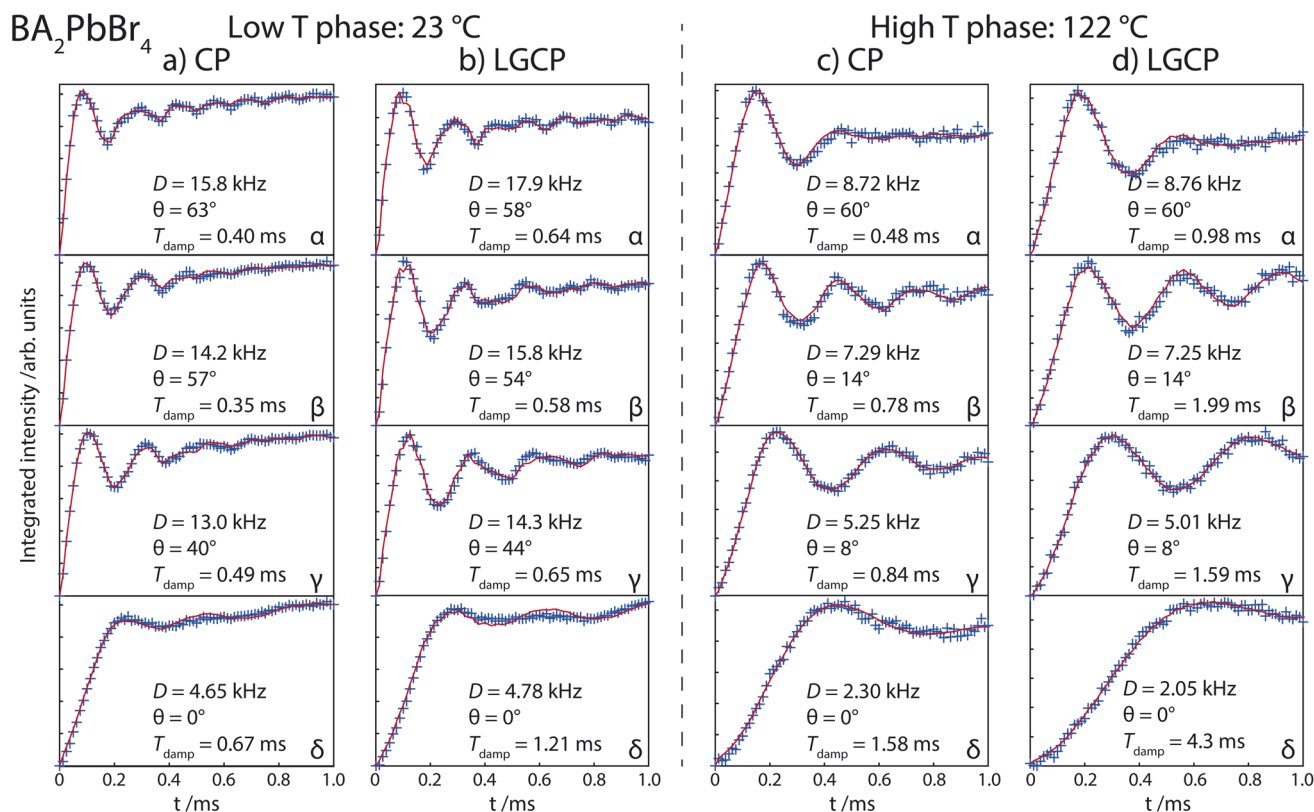
This journal is © The Royal Society of Chemistry 2025

J. Mater. Chem. A, 2025, **13**, 40153–40165 | **40157**

Fig. 7 Integrated intensity as a function of the $^1H \rightarrow {}^{13}C$ CP or LGCP contact time for each carbon in BA_2PbBr_4, above and below the quasi-melting phase transition. Experimental data are shown with blue crosses and fitted simulations with red lines. The carbons are labelled $\alpha-\delta$ where α is the $-CH_2-$ adjacent to the $-NH_3$ and δ is the $-CH_3$ group. Spectra were recorded at 11.7 T and 8 kHz MAS. Simulations were calculated using SIMPSON with the fitted parameters shown: D is the $^1H-^{13}C$ dipolar coupling, θ is the effective angle between the principal axes of the two $-CH_2-$ $^1H-^{13}C$ dipolar tensors, and T_{damp} is the time constant of the exponential decay applied to the simulated data.

near many halides in the inorganic layer, resulting in a distribution of different local environments. Peak splitting for the δ carbon was also previously observed by Lyu *et al.* in the low-temperature phases of pure-iodide $BA_2MA_{n-1}Pb_nI_{3n+1}$ with $n \geq$

2, which was ascribed to distinct "zigzag" and "extended" confirmations of BA^+;[41] however, they also observed clear splitting of the γ carbon, which is not the case here.
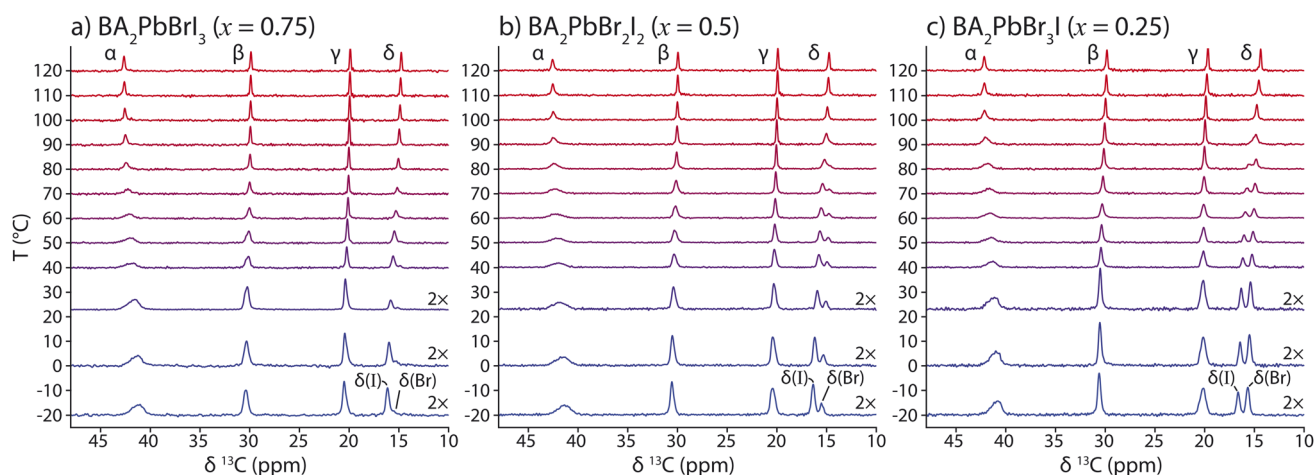

Fig. 8 $^1H \rightarrow {}^{13}C$ CP spectra of mixed-halide $BA_2Pb(Br_{1-x}I_x)_4$ as a function of temperature. Spectra were recorded at 11.7 T and 8 kHz MAS with a 1 ms contact time. The carbons are labelled $\alpha-\delta$ where α is the $-CH_2-$ adjacent to the $-NH_3$ and δ is the $-CH_3$ group, which can be adjacent to either axial iodide or bromide. The three lowest temperature spectra have been scaled vertically by a factor of two.
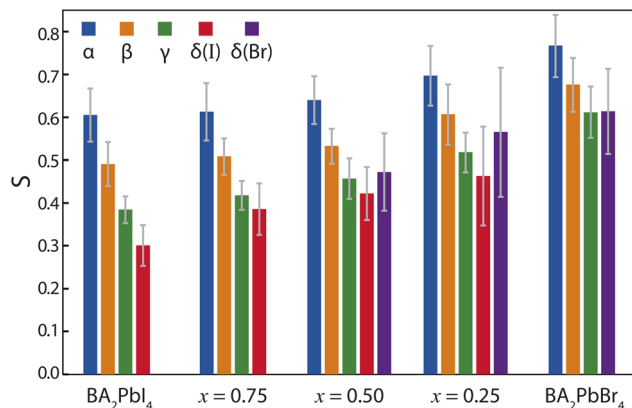
40158 | *J. Mater. Chem. A*, 2025, **13**, 40153–40165

This journal is © The Royal Society of Chemistry 2025

Fig. 9 Comparison of the ^{1}H–^{13}C order parameters, S, for pure and mixed-halide $BA_2Pb(Br_{1-x}I_x)_4$ 2D perovskites at room temperature as measured by fitting the LGCP build-up (Fig. 5, 7 and S7). The carbons are labelled α–δ where α is the –CH_2– adjacent to the –NH_3 and δ is the –CH_3 group, which can be adjacent to an axial iodide or bromide ion.

To interpret the peak narrowing, the linewidth of the α ^{13}C peak was plotted as a function of temperature for each sample and fitted using a phenomenological function[56,57] (Fig. S5 and Table S2). The temperature at which line narrowing occurs increases with increasing bromide content (Table S2); the inflection points are 68, 80, and 91 °C for $x = 0.75$, 0.5, and 0.25. Given that the inhomogeneous linewidth of the α carbon occurs due to a distribution of nearest neighbour halides, the narrowing implies that the carbon samples the different environments on a timescale faster than the linewidth (~175 Hz, ~2 ms). This could arise from translational diffusion of the BA^+ cation, diffusion of the halides, or both. Coalescence of the δ ^{13}C signals occurs at approximately the same temperatures as narrowing of the α resonance (Fig. 8), implying it is caused by the same process (the peak separation of ~120 Hz is comparable). The activation energies determined from this analysis (>1 eV; Table S) are higher than previously reported for halide exchange (0.75 eV),[27] therefore the narrowing is tentatively ascribed to exchange of the BA^+ cation. The activation energy increases with increasing bromide content, consistent with the higher onset temperature, which may be due to greater steric hindrance in the contracting unit cell.

To measure the extent of chain dynamics in the mixed-halide samples, the $^{1}H \rightarrow ^{13}C$ CP and LGCP build-up curves were measured at room temperature (Fig. S6, S7 and Tables S7–S9). All three samples show averaging of the ^{1}H–^{13}C dipolar coupling due to chain motion, with order parameters of $S = 0.4$–0.7 (Fig. 9 and Table S10) and reduced effective angles between the dipolar tensors. At room temperature, the pure iodide phase is above the quasi-melting transition, while the bromide is below. However, the chain dynamics of the mixed-halide samples are not clearly separated into quasi-melted and frozen regimes; instead, there is a continuous evolution of the order parameters in line with the sample composition, showing that mixed-halide 2D perovskites exhibit intermediate chain dynamics. As was observed for the end-members, the order parameter decreases

for progressive carbons moving away from the more constrained –NH_3^+ group. For the $x = 0.50$ and 0.25 samples where we can distinguish the signals from methyl carbons adjacent to axial iodide and bromide ions (δ(I) and δ(Br), respectively), S is larger for δ(Br), *i.e.*, more similar to the frozen bromide composition.

The experiments on the pure iodide and bromide samples show that the alkyl chains become more dynamic above the quasi-melting phase transition, while at a single temperature, mixed-halide samples show intermediate dynamics between those of the end-members. We now explore the temperature dependence more closely, to distinguish how much the chain dynamics evolve continuously as a function of temperature compared to the effect of the phase transition, and how this temperature dependence changes for mixed-halide samples. To improve sensitivity and avoid any effects of temperature-dependent ^{1}H pulse calibration, CP experiments were used rather than LGCP (Fig. S8–S12).

Fig. 10 shows the fitted order parameters as a function of temperature for all the samples. This reveals that the amplitude of chain motion increases progressively with temperature (*i.e.*, decreasing S) for all carbons of all samples. The concerted quasi-melting phase transitions in the pure iodide and bromide materials cause a jump in the order parameters significantly greater than the continuous temperature dependence, in line with the analysis above. The hysteresis in the phase transition for the iodide can be clearly distinguished. For the more constrained α and β carbons, S somewhat plateaus at the highest temperatures. Over the temperature range where the iodide is in the high-temperature quasi-melted phase and the bromide is in the low-temperature frozen phase, the amplitude of the chain dynamics for the mixed-halide samples is intermediate between the end-members in line with the composition (as was seen at room temperature above); however, below the phase transition, the iodide sample is more rigid than any of the mixed-halide samples. There is some evidence of greater dynamics for the bromide-rich $x = 0.25$ sample at 120 °C, which may correspond to a small quasi-melting transition at ~110 °C, which is just distinguishable in the DSC (Fig. 2). The effect of this transition is significantly smaller than for the end-members, and no corresponding jump in ^{13}C chemical shift was observed (Fig. 8). For the other mixed-halide samples, no phase transitions are observed, in line with the DSC and ^{13}C NMR spectra (see above).

Finally, having measured the amplitude of the chain dynamics, we briefly consider the timescale of chain motion. The ^{13}C T_1 relaxation is sensitive to both the amplitude and rate of fluctuations in the ^{1}H–^{13}C dipolar coupling. In the fast-motion regime ($1/\tau_c \gg \omega_0 = 125$ MHz), the ^{13}C T_1 is given by

$$\frac{1}{T_1} = N(1 - S)^2 (2\pi D_{rigid})^2 \tau_c, \tag{1}$$

where N is the number of bonded protons, S is the order parameter quantifying the amplitude of fluctuations of the dipolar coupling as discussed above, $D_{rigid} = 23.3$ kHz is the ^{1}H–^{13}C dipolar coupling constant in the absence of motion, and τ_c is a single representative correlation time of the motion in this model-free approach (see SI Note 2 for a derivation).[51,58–61]
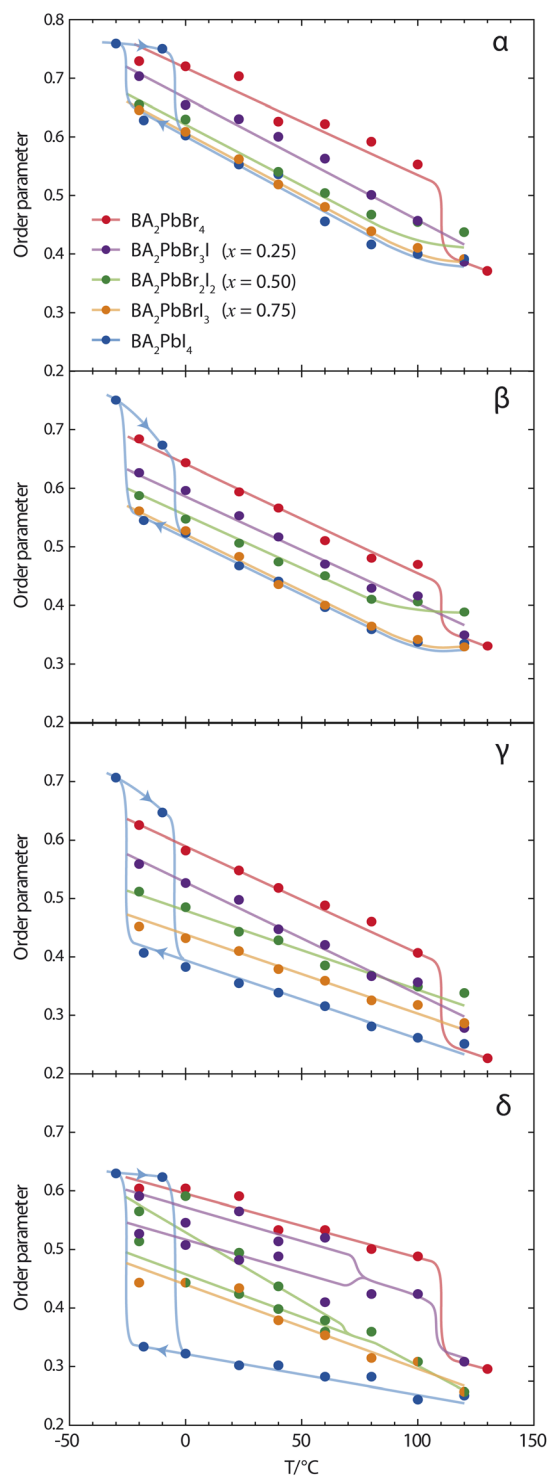
This journal is © The Royal Society of Chemistry 2025

J. Mater. Chem. A, 2025, **13**, 40153–40165 | **40159**

Fig. 10 ^{1}H–^{13}C order parameters (S) determined by fitting the CP build-up as a function of temperature for each carbon (α–δ) in BA$_2$Pb(Br$_{1-x}$I$_x$)$_4$ perovskites for $x = 0$, 0.25, 0.5, 0.75, and 1 (Fig. S8–S12). Solid lines are approximate guides to the eye. Where the two δ signals could be distinguished for mixed-halide samples, both are plotted. Error bars have been omitted for clarity, see Fig. S13 for separated plots with uncertainties. Note that due to the use of CP not LGCP, fewer scans, fewer points, and a shorter maximum build-up time (see Experimental), these data are less precise than the order parameters determined by LGCP above, but rather are intended to show the trends.

This can be understood as follows: the motion averages the dipolar coupling from D_{rigid} to $D = SD_{rigid}$, therefore during the motion the dipolar coupling fluctuates between D and D_{rigid}, *i.e.*, with an amplitude of $(D_{rigid} - D) = (1 - S)D_{rigid}$. For a discussion of the differences between this approach and the work of Landi *et al.*,[26] see SI Note 1.

Fig. 11a shows the ^{13}C T_1 relaxation of BA$_2$PbI$_4$ as a function of temperature. In the high-temperature phase, T_1 increases with increasing temperature, indicating that the motion is faster than the Larmor frequency. The –CH$_2$– carbons exhibit a jump to longer T_1 constants below the quasi-melting phase transition, with the expected hysteresis. We limit analysis to the –CH$_2$– groups since the –CH$_3$ relaxation also has a contribution from the fast C$_3$ rotation. Using eqn (1) and interpolating S from the measured order parameters by ^{1}H–^{13}C CP (see above), the correlation times were calculated (Fig. 11c). All three –CH$_2$– carbons exhibit very similar correlation times (~16 ps at room temperature, Table S4), indicating that the spread of T_1 values is predominantly due to the different amplitudes of motion (order parameters). Below the quasi-melting phase transition, the correlation times follow the same trend as in the room-temperature phase (Fig. 11c). This shows that the jump in the T_1 values is predominantly due to the change in the amplitude of motion (order parameter) across the phase transition, not a significant change in the correlation time for motion. Note that the decreasing –CH$_2$– T_1 values with increasing temperature in the low-temperature phase are due to the temperature dependence of S. There is some deviation from Arrhenius behaviour in the vicinity of the phase transition on heating, particularly for the α carbon, which is often encountered for first-order phase transitions.[62] The interpolation of S, especially below the transition, could also introduce error that may be responsible for the deviation. Arrhenius analysis yields activation energies in the range 0.12–0.15 eV (Table 2). The activation energies are similar for the three carbons, noting that there could be a large systematic error introduced from the order parameters. Interestingly, the activation energies appear to be the same above and below the transition, despite the large change in the amplitude of motion. We note that activation energies calculated directly from the T_1 values are significantly different due to the temperature dependence of the order parameters for the motion.

Similar results are observed for the ^{13}C T_1 relaxation of BA$_2$-PbBr$_4$ (Fig. 11b), with a jump across the phase transition. The correlation times are slightly longer than for BA$_2$PbI$_4$, ~24 ps at room temperature (Table S5). The correlation times also exhibit Arrhenius behaviour (Fig. 11d), although the β and γ carbons do not fit the trend above the phase transition; higher temperature data would be required to establish if this is due to consistently faster motion in the high-temperature phase, or deviation in the vicinity of the phase transition. Slightly lower activation energies of $E_a = 0.10$–0.12 eV are observed (Table 2). Full variable-temperature relaxometry was not performed for the mixed-halide samples, but the room-temperature correlation times are similar to the end-members (Tables S7–S9 and S11).
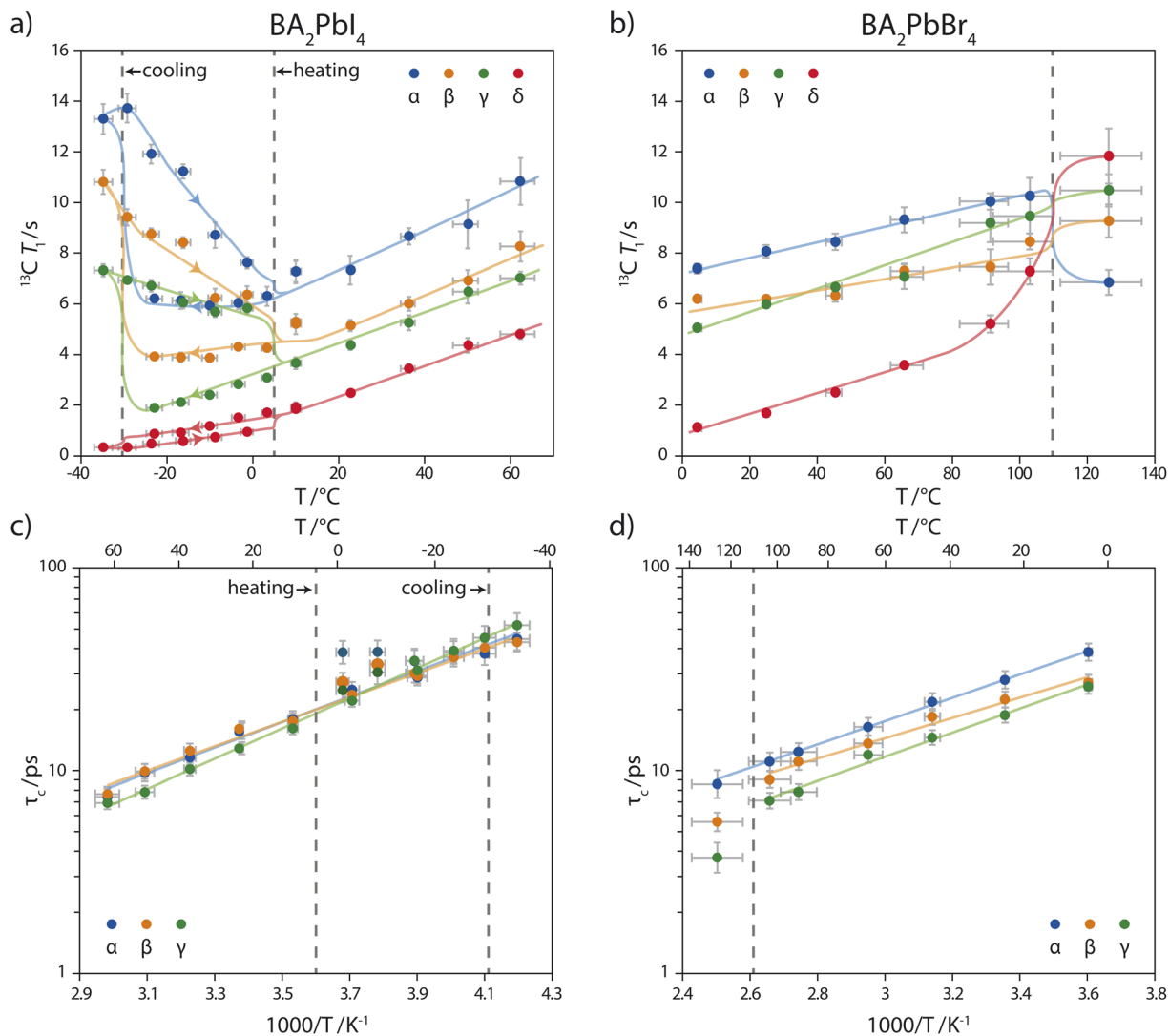
40160 | *J. Mater. Chem. A*, 2025, **13**, 40153–40165

This journal is © The Royal Society of Chemistry 2025

Fig. 11 (a and b) ^{13}C T_1 constants for BA_2PbI_4 and BA_2PbBr_4 as a function of temperature. Solid lines are guides to the eye. Vertical lines indicate the phase transitions. (c and d) Arrhenius plot of the correlation times, τ_c, calculated from the ^{13}C T_1 values and ^1H–^{13}C dipolar order parameters; see main text. Solid lines are linear fits; for BA_2PbI_4, the outliers below the transition on heating were excluded, for BA_2PbBr_4, only the points below the transition were included. The carbons of BA^+ are labelled α–δ, moving away from the $-NH_3$ group.

Table 2 Activation energies for motion of the $-CH_2-$ carbons in BA_2PbI_4 and BA_2PbBr_4 from Arrhenius analysis of the correlations times calculated from ^{13}C T_1 values and ^1H–^{13}C order parameters. Errors are estimated from Monte Carlo analysis using the uncertainties in the temperature and τ_c values

E_a/eV	α	β	γ
BA_2PbI_4	0.125 ± 0.007	0.120 ± 0.006	0.148 ± 0.007
BA_2PbBr_4	0.114 ± 0.010	0.100 ± 0.010	0.118 ± 0.009

Conclusions

In summary, the amplitude of the chain dynamics in BA^+-based 2D mixed-halide lead perovskites ($BA_2Pb(Br_{1-x}I_x)_4$) has been quantified *via* the partial averaging of the ^1H–^{13}C dipolar

coupling using variable temperature CP and LGCP build-up experiments. The ammonium end of the molecule is more constrained by bonding with the inorganic perovskite layer, and the carbons become increasingly dynamic moving down the chain. The amplitude of cation motion increases with increasing temperature, with a significant jump across the quasi-melting phase transitions in pure BA_2PbI_4 and BA_2PbBr_4. These phase transitions also cause a jump in the ^{13}C chemical shifts. Combining the order parameters from the CP build-up with ^{13}C T_1 data enables the correlation times and activation energies for the cation motion to be calculated, on the order of $\sim$20 ps at room temperature and $\sim$0.1 eV, respectively.

Concerted quasi-melting phase transitions of the cations are suppressed by halide mixing. Between -20 °C and 120 °C, there are no jumps in the ^{13}C chemical shifts. The amplitude of the chain motion for the mixed-halide samples is intermediate between that of the end-members, rather than resembling

This journal is © The Royal Society of Chemistry 2025

J. Mater. Chem. A, 2025, **13**, 40153–40165 | **40161**

either the quasi-melted iodide or quasi-frozen bromide phases, while the correlation times are similar. Like the end-members, the motional amplitude increases continuously with increasing temperature. BA_2PbBrI_3 and $BA_2PbBr_2I_2$ samples exhibited no jumps in motional amplitude over this temperature range, while BA_2PbBr_3I showed only a slight jump, indicating that the phase transitions are partly or fully suppressed, in line with DSC measurements.

The suppression of concerted phase transitions of the cation dynamics is ascribed to the range of local environments resulting from (partial) halide disorder. In each environment, the cation experiences different steric and bonding constraints, that would result in a different quasi-melting temperature, rather than a single well-defined transition as for the pure halide materials. The disorder is reflected in the broadening and splitting of the ^{13}C signals for the mixed-halide samples. Dynamical averaging of this disorder occurs at elevated temperatures, which is attributed to diffusion of BA^+ cations, with activation energies of 1–1.6 eV as determined by lineshape analysis.

Overall, this detailed analysis demonstrates the power of NMR spectroscopy to quantify the rate and amplitude of molecular motion in complex hybrid materials. Since the chain dynamics modulate the physical and optoelectronic properties, this information can inform the design of spacer molecules for layered perovskite photovoltaics and passivating layers, especially for wide-bandgap mixed-halide or otherwise disordered systems.

Experimental

Samples were prepared by mechanosynthesis with appropriate ratios of BABr, BAI, $PbBr_2$, and PbI_2, before annealing at 150 °C for 30 minutes, as described in Hope et al.[44] Phase purity was confirmed by powder XRD (Fig. S1) using a Bruker D8 Discover Vario diffractometer with monochromatic Cu Kα_1 radiation (1.5406 Å). A single sample was prepared for each composition. The error in the halide composition of the mixed-halide samples is estimated as ±3% based on previous determination of the unit cell volume and agreement with Vegard's law.[44] Previous ^{207}Pb NMR results on these samples indicate a homogeneous halide distribution (although there is a preference for iodide to occupy the axial site).[44] Differential scanning calorimetry was performed with a Mettler Toledo DSC 1 equipped with liquid nitrogen cooling. Samples were run in 40 μl aluminium pans under a nitrogen atmosphere (50 ml min^{-1} flow rate), measuring the heat flow relative to a reference pan. Experiments were performed between −150 and 210 °C, at 20 °C min^{-1}, with a 5 minutes isotherm between each run. Structures were visualised using VESTA.[63]

NMR spectra were recorded at 11.7 T and 8 kHz MAS using a double resonance probe, 3.2 mm ZrO_2 rotors, and either a Bruker Avance III or Avance Neo spectrometer. Ex situ temperature calibration was performed using the temperature-dependent ^{207}Pb signal of $Pb(NO_3)_2$; the width of the ^{207}Pb signal was used to determine the temperature gradients within the rotor, which are shown as error bars in the corresponding plots.[64] ^{13}C spectra were referenced to the CH adamantane signal at 37.78 ppm at room temperature.[65] CP experiments were performed with radiofrequency strengths of 50 kHz and 58 kHz for ^{13}C and ^1H; for LGCP experiments, the ^1H radiofrequency strength was reduced by $\sqrt{2/3}$ to 47.4 kHz with an offset of +33.5 kHz. LGCP experiments used a 90° ^1H excitation pulse so that it could be phase cycled to remove background, at the expense of some signal reduction.[48] 1D $^1H \rightarrow ^{13}C$ CP spectra were recorded with a 1 ms contact time and a 90–100% ramp on the ^1H power. (LG)CP build-up curves were measured without a ramp in steps of 12.5 μs up to 1 ms; experimental times were 4–10 hours. Variable temperature CP build-up curves in Fig. 10 were measured in steps of 25 μs up to 600 or 800 μs with experimental times of 15–45 minutes. Recycle delays of 1–10 s were used, based on the measured ^1H T_1 which increases with increasing temperature. 70–80 kHz of SPINAL64 ^1H decoupling was applied during acquisition. ^{13}C T_1 relaxation was measured using the Torchia experiment: $^1H \rightarrow ^{13}C$ CP is followed by a ^{13}C 90° pulse that stores the magnetisation on ±z for a variable delay; storage alternates between +z and −z to cancel the thermal magnetisation.[66] The delay list was 0.1, 0.2, 0.45, 1, 2, 4.5, 10, 20, 45, 100 s; the end-members were recorded with 4 scans while mixed-halide samples had up to 64 scans. T_1 data were fitted with a single exponential decay and the errors estimated using Monte Carlo analysis based on the root-mean-squared error (RMSE) between the experimental data and the best fit. Variable temperature $^1H \rightarrow ^{13}C$ CP spectra were deconvoluted with dmfit.[67]

The integrated (LG)CP intensity was fitted as a function of CP contact time (t) using SIMPSON with 168 crystallites (rep168 scheme) and 16 gamma angles per rotor period.[47,52] The build-up curve was simulated for a given ^1H–^{13}C dipolar coupling strength (D) and, for –CH_2– groups, a given effective angle (θ) between the two dipolar tensors of that –CH_2–. The simulated data, $I(t)$, was then scaled and a damping function applied using the following equation:

$$I_{\text{damped}}(t) = A\left[(I(t) - I_0)\exp\left(-\frac{t}{T_{\text{damp}}}\right) + I_0\right],$$

where A is the overall scaling, T_{damp} is the time constant for damping, and I_0 is the plateaued intensity at long time. These three parameters were optimised to give the best fit to the experimental data for each simulated build-up curve. D and θ were then optimised, simulating the build-up at each step, to give the best fit to the experimental data. Note that the LGCP simulations include the ^1H offset during cross polarisation and therefore account for the scaling of the dipolar coupling by $1/\sqrt{3}$; no manual scaling is necessary. The uncertainty in the fitted dipolar coupling was estimated by varying D around the optimised value (D^*) by ±500 Hz in steps of 50 Hz, at each step optimising the other fitting parameters, then calculating the RMSE, $\sigma(D)$, and fitting to a quadratic function:

$$\sigma(D) = a(D - D^*)^2 + b(D - D^*) + c$$

The uncertainty in D is then approximated by

40162 | J. Mater. Chem. A, 2025, **13**, 40153–40165

This journal is © The Royal Society of Chemistry 2025

$$\Delta D = \sqrt{\frac{c}{a}}$$

This method likely overestimates the error because the RMSE is calculated over the whole measured data, but the build-up curve is most sensitive to the dipolar coupling at short times.

Conflicts of interest

There are no conflicts to declare.

Data availability

Raw and processed data as well as SIMPSON scripts are available at DOI: https://doi.org/10.5281/zenodo.15829934.

Additional figures, tables, and discussion are available in the supplementary information(SI). See DOI: https://doi.org/10.1039/d5ta06091e.

Acknowledgements

References

1 P. Gao, M. Grätzel and M. K. Nazeeruddin, Organohalide lead perovskites for photovoltaic applications, *Energy Environ. Sci.*, 2014, **7**(8), 2448–2463, DOI: 10.1039/c4ee00942h.

2 S. D. Stranks and H. J. Snaith, Metal-halide perovskites for photovoltaic and light-emitting devices, *Nat. Nanotechnol.*, 2015, **10**(5), 391–402, DOI: 10.1038/nnano.2015.90.

3 B. Saparov and D. B. Mitzi, Organic–Inorganic Perovskites: Structural Versatility for Functional Materials Design, *Chem. Rev.*, 2016, **116**(7), 4558–4596, DOI: 10.1021/acs.chemrev.5b00715.

4 J.-P. Correa-Baena, M. Saliba, T. Buonassisi, M. Grätzel, A. Abate, W. Tress and A. Hagfeldt, Promises and challenges of perovskite solar cells, *Science*, 2017, **358**(6364), 739–744, DOI: 10.1126/science.aam6323.

5 A. K. Jena, A. Kulkarni and T. Miyasaka, Halide Perovskite Photovoltaics: Background, Status, and Future Prospects, *Chem. Rev.*, 2019, **119**(5), 3036–3103, DOI: 10.1021/acs.chemrev.8b00539.

6 J. Y. Kim, J.-W. Lee, H. S. Jung, H. Shin and N.-G. Park, High-Efficiency Perovskite Solar Cells, *Chem. Rev.*, 2020, **120**(15), 7867–7918, DOI: 10.1021/acs.chemrev.0c00107.

7 M. Simenas, A. Gagor, J. Banys and M. Maczka, Phase Transitions and Dynamics in Mixed Three- and Low-Dimensional Lead Halide Perovskites, *Chem. Rev.*, 2024, **124**(5), 2281–2326, DOI: 10.1021/acs.chemrev.3c00532.

8 H. Tsai, W. Nie, J.-C. Blancon, C. C. Stoumpos, R. Asadpour, B. Harutyunyan, A. J. Neukirch, R. Verduzco, J. J. Crochet, S. Tretiak, L. Pedesseau, J. Even, M. A. Alam, G. Gupta, J. Lou, P. M. Ajayan, M. J. Bedzyk, M. G. Kanatzidis and A. D. Mohite, High-efficiency two-dimensional Ruddlesden–Popper perovskite solar cells, *Nature*, 2016, **536**(7616), 312–316, DOI: 10.1038/nature18306.

9 Z. Wang, Q. Lin, F. P. Chmiel, N. Sakai, L. M. Herz and H. J. Snaith, Efficient ambient-air-stable solar cells with 2D–3D heterostructured butylammonium-caesium-formamidinium lead halide perovskites, *Nat. Energy*, 2017, **2**, 17135, DOI: 10.1038/nenergy.2017.135.

10 G. Grancini, C. Roldán-Carmona, I. Zimmermann, E. Mosconi, X. Lee, D. Martineau, S. Narbey, F. Oswald, F. De Angelis, M. Graetzel and M. K. Nazeeruddin, One-Year stable perovskite solar cells by 2D/3D interface engineering, *Nat. Commun.*, 2017, **8**, 15684, DOI: 10.1038/ncomms15684.

11 G. Grancini and M. K. Nazeeruddin, Dimensional tailoring of hybrid perovskites for photovoltaics, *Nat. Rev. Mater.*, 2018, **4**(1), 4–22, DOI: 10.1038/s41578-018-0065-0.

12 P. Chen, Y. Bai, S. Wang, M. Lyu, J. H. Yun and L. Wang, In Situ Growth of 2D Perovskite Capping Layer for Stable and Efficient Perovskite Solar Cells, *Adv. Funct. Mater.*, 2018, **28**, 1706923, DOI: 10.1002/adfm.201706923.

13 Y. Liu, S. Akin, A. Hinderhofer, F. T. Eickemeyer, H. Zhu, J. Y. Seo, J. Zhang, F. Schreiber, H. Zhang, S. M. Zakeeruddin, A. Hagfeldt, M. I. Dar and M. Grätzel, Stabilization of Highly Efficient and Stable Phase-Pure FAPbI$_3$ Perovskite Solar Cells by Molecularly Tailored 2D-Overlayers, *Angew. Chem., Int. Ed.*, 2020, **59**(36), 15688–15694, DOI: 10.1002/anie.202005211.

14 X. Li, J. M. Hoffman and M. G. Kanatzidis, The 2D Halide Perovskite Rulebook: How the Spacer Influences Everything from the Structure to Optoelectronic Device Efficiency, *Chem. Rev.*, 2021, **121**(4), 2230–2291, DOI: 10.1021/acs.chemrev.0c01006.

15 S. Barman, N. V. Venkataraman, S. Vasudevan and R. Seshadri, Phase Transitions in the Anchored Organic Bilayers of Long-Chain Alkylammonium Lead Iodides $(C_nH_{2n+1}NH_3)_2PbI_4$; n = 12, 16, 18, *J. Phys. Chem. B*, 2003, **107**(8), 1875–1883, DOI: 10.1021/jp026879h.

16 D. G. Billing and A. Lemmerer, Synthesis, characterization and phase transitions in the inorganic–organic layered perovskite-type hybrids $[(C_nH_{2n+1}NH_3)_2PbI_4]$, n = 4, 5 and 6, *Acta Crystallogr., Sect. B*, 2007, **63**(5), 735–747, DOI: 10.1107/s0108768107031758.

17 H. Abid, A. Trigui, A. Mlayah, E. K. Hlil and Y. Abid, Phase transition in organic–inorganic perovskite $(C_9H_{19}NH_3)_2PbI_2Br_2$ of long-chain alkylammonium, *Results Phys.*, 2012, **2**, 71–76, DOI: 10.1016/j.rinp.2012.04.003.

18 N. S. Dahod, W. Paritmongkol, A. Stollmann, C. Settens, S.-L. Zheng and W. A. Tisdale, Melting Transitions of the

This journal is © The Royal Society of Chemistry 2025

J. Mater. Chem. A, 2025, **13**, 40153–40165 | **40163**

Organic Subphase in Layered Two-Dimensional Halide Perovskites, *J. Phys. Chem. Lett.*, 2019, **10**(11), 2924–2930, DOI: 10.1021/acs.jpclett.9b00983.

19 D. Cortecchia, S. Neutzner, J. Yin, T. Salim, A. R. Srimath Kandada, A. Bruno, Y. M. Lam, J. Martí-Rujas, A. Petrozza and C. Soci, Structure-controlled optical thermoresponse in Ruddlesden-Popper layered perovskites, *APL Mater.*, 2018, **6**, 114207, DOI: 10.1063/1.5045782.

20 T. Li, W. A. Dunlap-Shohl, E. W. Reinheimer, P. Le Magueres and D. B. Mitzi, Melting temperature suppression of layered hybrid lead halide perovskites via organic ammonium cation branching, *Chem. Sci.*, 2019, **10**(4), 1168–1175, DOI: 10.1039/c8sc03863e.

21 Q. Q. Jia, L. Tong, W. Y. Zhang, D. W. Fu and H. F. Lu, Two-Step Dielectric Responsive Organic-Inorganic Hybrid Material with Mid-Band Light Emission, *Chem. Eur J.*, 2022, **28**(40), e202200579, DOI: 10.1002/chem.202200579.

22 Q.-Q. Jia, L. Tong, M.-M. Lun, D.-W. Fu, T. Zhang and H.-F. Lu, Two-Dimensional Organic–Inorganic Hybrid Materials with Dielectric Switching and Photoluminescence Properties, *Cryst. Growth Des.*, 2022, **22**(5), 2799–2805, DOI: 10.1021/acs.cgd.2c00183.

23 R.-I. Biega, M. Bokdam, K. Herrmann, J. Mohanraj, D. Skrybeck, M. Thelakkat, M. Retsch and L. Leppert, Dynamic Distortions of Quasi-2D Ruddlesden–Popper Perovskites at Elevated Temperatures: Influence on Thermal and Electronic Properties, *J. Phys. Chem. C*, 2023, **127**(19), 9183–9195, DOI: 10.1021/acs.jpcc.3c01634.

24 R. Namakian, M. A. Garzon, Q. Tu, A. Erdemir and W. Gao, Temperature-Induced Phase Transition in 2D Alkylammonium Lead Halide Perovskites: A Molecular Dynamics Study, *ACS Nano*, 2024, **18**(34), 22926–22937, DOI: 10.1021/acsnano.4c03903.

25 X. Gong, O. Voznyy, A. Jain, W. Liu, R. Sabatini, Z. Piontkowski, G. Walters, G. Bappi, S. Nokhrin, O. Bushuyev, M. Yuan, R. Comin, D. McCamant, S. O. Kelley and E. H. Sargent, Electron–phonon interaction in efficient perovskite blue emitters, *Nat. Mater.*, 2018, **17**(6), 550–556, DOI: 10.1038/s41563-018-0081-x.

26 N. Landi, D. Marongiu, S. Borsacchi, L. Calucci, E. Maurina, S. Lai, R. Pau, A. Simbula, M. Saba, M. Geppi and E. Carignani, Dynamic Disorder in Monolayer and Multilayer 2D Ruddlesden–Popper Lead Iodide Perovskites: Evidence from Solid-State Nuclear Magnetic Resonance and Ultrafast Optical Spectroscopy, *Chem. Mater.*, 2024, **36**(18), 8725–8736, DOI: 10.1021/acs.chemmater.4c01413.

27 J. Cho, J. T. DuBose, A. N. T. Le and P. V. Kamat, Suppressed Halide Ion Migration in 2D Lead Halide Perovskites, *ACS Mater. Lett.*, 2020, **2**(6), 565–570, DOI: 10.1021/acsmaterialslett.0c00124.

28 P. S. Mathew, J. T. DuBose, J. Cho and P. V. Kamat, Spacer Cations Dictate Photoinduced Phase Segregation in 2D Mixed Halide Perovskites, *ACS Energy Lett.*, 2021, **6**(7), 2499–2501, DOI: 10.1021/acsenergylett.1c01015.

29 J. Cho, P. S. Mathew, J. T. DuBose and P. V. Kamat, Photoinduced Halide Segregation in Ruddlesden–Popper 2D Mixed Halide Perovskite Films, *Adv. Mater.*, 2021, **33**(48), 2105585, DOI: 10.1002/adma.202105585.

30 K. Datta, A. Caiazzo, M. A. Hope, J. Li, A. Mishra, M. Cordova, Z. Chen, L. Emsley, M. M. Wienk and R. A. J. Janssen, Light-Induced Halide Segregation in 2D and Quasi-2D Mixed-Halide Perovskites, *ACS Energy Lett.*, 2023, **8**(4), 1662–1670, DOI: 10.1021/acsenergylett.3c00160.

31 B. Reif, S. E. Ashbrook, L. Emsley and M. Hong, Solid-state NMR spectroscopy, *Nat. Rev. Methods Primers*, 2021, **1**(1), 2, DOI: 10.1038/s43586-020-00002-1.

32 W. M. J. Franssen and A. P. M. Kentgens, Solid–state NMR of hybrid halide perovskites, *Solid State Nucl. Magn. Reson.*, 2019, **100**, 36–44, DOI: 10.1016/j.ssnmr.2019.03.005.

33 L. Piveteau, V. Morad and M. V. Kovalenko, Solid-State NMR and NQR Spectroscopy of Lead-Halide Perovskite Materials, *J. Am. Chem. Soc.*, 2020, **142**(46), 19413–19437, DOI: 10.1021/jacs.0c07338.

34 D. J. Kubicki, S. D. Stranks, C. P. Grey and L. Emsley, NMR spectroscopy probes microstructure, dynamics and doping of metal halide perovskites, *Nat. Rev. Chem.*, 2021, **5**(9), 624–645, DOI: 10.1038/s41570-021-00309-x.

35 G. M. Bernard, R. E. Wasylishen, C. I. Ratcliffe, V. Terskikh, Q. Wu, J. M. Buriak and T. Hauger, Methylammonium Cation Dynamics in Methylammonium Lead Halide Perovskites: A Solid-State NMR Perspective, *J. Phys. Chem. A*, 2018, **122**(6), 1560–1573, DOI: 10.1021/acs.jpca.7b11558.

36 C. Roiland, G. Trippé-Allard, K. Jemli, B. Alonso, J.-C. Ameline, R. Gautier, T. Bataille, L. Le Pollès, E. Deleporte, J. Even and C. Katan, Multinuclear NMR as a tool for studying local order and dynamics in $CH_3NH_3PbX_3(X = Cl, Br, I)$ hybrid perovskites, *Phys. Chem. Chem. Phys.*, 2016, **18**(39), 27133–27142, DOI: 10.1039/c6cp02947g.

37 D. H. Fabini, T. A. Siaw, C. C. Stoumpos, G. Laurita, D. Olds, K. Page, J. G. Hu, M. G. Kanatzidis, S. Han and R. Seshadri, Universal Dynamics of Molecular Reorientation in Hybrid Lead Iodide Perovskites, *J. Am. Chem. Soc.*, 2017, **139**(46), 16875–16884, DOI: 10.1021/jacs.7b09536.

38 A. Mishra, M. A. Hope, M. Grätzel and L. Emsley, A Complete Picture of Cation Dynamics in Hybrid Perovskite Materials from Solid-State NMR Spectroscopy, *J. Am. Chem. Soc.*, 2022, **145**(2), 978–990, DOI: 10.1021/jacs.2c10149.

39 Y. Dou, Q. Wang, H. Ji and H. Liu, Probing cation dynamics and phase transition in hybrid organic-inorganic perovskites by ^{13}C solid-state NMR spectroscopy at very high resolution, *Open Magn. Reson. J.*, 2025, **23**, 100197, DOI: 10.1016/j.jmro.2025.100197.

40 J. Lee, W. Lee, K. Kang, T. Lee and S. K. Lee, Layer-by-Layer Structural Identification of 2D Ruddlesden–Popper Hybrid Lead Iodide Perovskites by Solid-State NMR Spectroscopy, *Chem. Mater.*, 2020, **33**(1), 370–377, DOI: 10.1021/acs.chemmater.0c04078.

41 F. Lyu, X. Zheng, Z. Li, Z. Chen, R. Shi, Z. Wang, H. Liu and B.-L. Lin, Spatiodynamics, Photodynamics, and Their Correlation in Hybrid Perovskites, *Chem. Mater.*, 2021, **33**(10), 3524–3533, DOI: 10.1021/acs.chemmater.0c04500.

40164 | *J. Mater. Chem. A*, 2025, **13**, 40153–40165

This journal is © The Royal Society of Chemistry 2025

42 C.-C. Lin, S.-J. Huang, P.-H. Wu, T.-P. Chen, C.-Y. Huang, Y.-C. Wang, P.-T. Chen, D. Radeva, O. Petrov, V. M. Gelev, R. Sankar, C.-C. Chen, C.-W. Chen and T.-Y. Yu, Direct investigation of the reorientational dynamics of A-site cations in 2D organic-inorganic hybrid perovskite by solid-state NMR, *Nat. Commun.*, 2022, **13**, 1513, DOI: **10.1038/s41467-022-29207-6**.

43 T. Ueda, K. Shimizu, H. Ohki and T. Okuda, ^{13}C CP/MAS NMR Study of the Layered Compounds $[C_6H_5CH_2CH_2NH_3]_2[CH_3NH_3]_{n-1}Pb_nI_{3n+1}$ (n = 1, 2), *Z. Naturforsch., A*, 1996, **51**(8), 910–914, DOI: **10.1515/zna-1996-0805**.

44 M. A. Hope, M. Cordova, A. Mishra, U. Gunes, A. Caiazzo, K. Datta, R. A. J. Janssen and L. Emsley, Axial–Equatorial Halide Ordering in Layered Hybrid Perovskites from Isotropic–Anisotropic ^{207}Pb NMR, *Angew. Chem., Int. Ed.*, 2024, **63**(13), e202314856, DOI: **10.1002/anie.202314856**.

45 L. Müller, A. Kumar, T. Baumann and R. R. Ernst, Transient Oscillations in NMR Cross-Polarization Experiments in Solids, *Phys. Rev. Lett.*, 1974, **32**(25), 1402–1406, DOI: **10.1103/PhysRevLett.32.1402**.

46 D. C. Apperley, R. K. Harris and P. Hodgkinson, *Solid-State NMR : Basic Principles and Practice*, Momentum Press, 2012.

47 S. K. Mann, M. K. Devgan, W. T. Franks, S. Huband, C. L. Chan, J. Griffith, D. Pugh, N. J. Brooks, T. Welton, T. N. Pham, L. L. McQueen, J. R. Lewandowski and S. P. Brown, MAS NMR Investigation of Molecular Order in an Ionic Liquid Crystal, *J. Phys. Chem. B*, 2020, **124**(24), 4975–4988, DOI: **10.1021/acs.jpcb.0c02328**.

48 B. J. van Rossum, C. P. de Groot, V. Ladizhansky, S. Vega and H. J. M. de Groot, A Method for Measuring Heteronuclear (^{1}H–^{13}C) Distances in High Speed MAS NMR, *J. Am. Chem. Soc.*, 2000, **122**(14), 3465–3472, DOI: **10.1021/ja992714j**.

49 M. Hong, X. Yao, K. Jakes and D. Huster, Investigation of Molecular Motions by Lee-Goldburg Cross-Polarization NMR Spectroscopy, *J. Phys. Chem. B*, 2002, **106**(29), 7355–7364, DOI: **10.1021/jp0156064**.

50 J. J. Kinnun, A. Leftin and M. F. Brown, Solid-State NMR Spectroscopy for the Physical Chemistry Laboratory, *J. Chem. Educ.*, 2012, **90**(1), 123–128, DOI: **10.1021/ed2004774**.

51 G. Lipari and A. Szabo, Model-free approach to the interpretation of nuclear magnetic resonance relaxation in macromolecules. 1. Theory and range of validity, *J. Am. Chem. Soc.*, 2002, **104**(17), 4546–4559, DOI: **10.1021/ja00381a009**.

52 M. Bak, J. T. Rasmussen and N. C. Nielsen, SIMPSON.: A General Simulation Program for Solid-State NMR Spectroscopy, *J. Magn. Reson.*, 2000, **147**(2), 296–330, DOI: **10.1006/jmre.2000.2179**.

53 S. Toso, I. Gushchina, A. G. Oliver, L. Manna and M. Kuno, Are Mixed-Halide Ruddlesden–Popper Perovskites Really Mixed?, *ACS Energy Lett.*, 2022, **7**(12), 4242–4247, DOI: **10.1021/acsenergylett.2c01967**.

54 N. E. Wright, X. Qin, J. Xu, L. L. Kelly, S. P. Harvey, M. F. Toney, V. Blum and A. D. Stiff-Roberts, Influence of Annealing and Composition on the Crystal Structure of Mixed-Halide, Ruddlesden–Popper Perovskites, *Chem. Mater.*, 2022, **34**(7), 3109–3122, DOI: **10.1021/acs.chemmater.1c04213**.

55 Z. Chen, H. Xue, G. Brocks, P. A. Bobbert and S. Tao, Thermodynamic Origin of the Photostability of the Two-Dimensional Perovskite $PEA_2Pb(I_{1-x}Br_x)_4$, *ACS Energy Lett.*, 2023, **8**(2), 943–949, DOI: **10.1021/acsenergylett.2c02463**.

56 J. R. Hendrickson and P. J. Bray, A phenomenological equation for NMR motional narrowing in solids, *J. Magn. Reson.*, 1973, **9**(3), 341–357, DOI: **10.1016/0022-2364(73)90176-5**.

57 M. Wilkening, D. Bork, S. Indris and P. Heitjans, Diffusion in amorphous $LiNbO_3$ studied by ^{7}Li NMR — comparison with the nano- and microcrystalline material, *Phys. Chem. Chem. Phys.*, 2002, **4**(14), 3246–3251, DOI: **10.1039/b201193j**.

58 Z. L. Gasyna and A. Jurkiewicz, Determination of Spin—Lattice Relaxation Time Using 13C NMR. An Undergraduate Physical Chemistry Laboratory Experiment, *J. Chem. Educ.*, 2004, **81**(7), 1038, DOI: **10.1021/ed081p1038**.

59 V. Chevelkov, U. Fink and B. Reif, Quantitative analysis of backbone motion in proteins using MAS solid-state NMR spectroscopy, *J. Biomol. NMR*, 2009, **45**(1–2), 197–206, DOI: **10.1007/s10858-009-9348-5**.

60 J. R. Lewandowski, M. E. Halse, M. Blackledge and L. Emsley, Direct observation of hierarchical protein dynamics, *Science*, 2015, **348**(6234), 578–581, DOI: **10.1126/science.aaa6111**.

61 A. A. Smith, E. Testori, R. Cadalbert, B. H. Meier and M. Ernst, Characterization of fibril dynamics on three timescales by solid-state NMR, *J. Biomol. NMR*, 2016, **65**(3–4), 171–191, DOI: **10.1007/s10858-016-0047-8**.

62 K. R. Jeffrey and G. H. Penner, *Structural Phase Transitions*, ed R. K. Harris and R. E. Wasylishen, eMagRes, 2009.

63 K. Momma and F. Izumi, VESTA 3for three-dimensional visualization of crystal, volumetric and morphology data, *J. Appl. Crystallogr.*, 2011, **44**(6), 1272–1276, DOI: **10.1107/s0021889811038970**.

64 A. Bielecki and D. P. Burum, Temperature Dependence of ^{207}Pb MAS Spectra of Solid Lead Nitrate. An Accurate, Sensitive Thermometer for Variable-Temperature MAS, *J. Magn. Reson., Ser. A*, 1995, **116**(2), 215–220, DOI: **10.1006/jmra.1995.0010**.

65 R. Hoffman, Solid-state chemical-shift referencing with adamantane, *J. Magn. Reson.*, 2022, **340**, 107231, DOI: **10.1016/j.jmr.2022.107231**.

66 D. A. Torchia, The measurement of proton-enhanced carbon-13 T_1 values by a method which suppresses artifacts, *J. Magn. Reson.*, 1978, **30**(3), 613–616, DOI: **10.1016/0022-2364(78)90288-3**.

67 D. Massiot, F. Fayon, M. Capron, I. King, S. Le Calvé, B. Alonso, J. O. Durand, B. Bujoli, Z. Gan and G. Hoatson, Modelling one- and two-dimensional solid-state NMR spectra, *Magn. Reson. Chem.*, 2001, **40**(1), 70–76, DOI: **10.1002/mrc.984**.

This journal is © The Royal Society of Chemistry 2025

J. Mater. Chem. A, 2025, **13**, 40153–40165 | **40165**